Bonding states underpinning structural transitions in IrTe2 observed with micro-ARPES

Christopher W. Nicholson, Matthew D Watson, Aki Pulkkinen, Maxime Rumo, Geoffroy Kremer, Keyuan Ma, Fabian O. von Rohr, Céphise Cacho, Claude Monney

Editors' Suggestion

Bonding states underpinning structural transitions in $IrTe_2$ observed with micro-ARPES

C. W. Nicholson,[1,2,*] M. D. Watson,[3] A. Pulkkinen,[1,4] M. Rumo,[1] G. Kremer,[1,5] K. Y. Ma,[6] F. O. von Rohr,[7] C. Cacho,[3] and C. Monney[1,†]

[1]*University of Fribourg and Fribourg Centre for Nanomaterials, Chemin du Musée 3, CH-1700 Fribourg, Switzerland*
[2]*Fritz-Haber-Institut der Max-Planck-Gesellscahft, Faradayweg 4-6, D-14195 Berlin, Germany*
[3]*Diamond Light Source, Ltd., Harwell Science and Innovation Campus, Didcot, Oxfordshire OX110DE, England, United Kingdom*
[4]*New Technologies-Research Center, University of West Bohemia, Plzeň 301 00, Czech Republic*
[5]*Institut Jean Lamour, UMR 7198, Centre National de la Recherche Scientifique–Université de Lorraine, Campus ARTEM, 2 Allée André Guinier, BP 50840, 54011 Nancy, France*
[6]*Max Planck Institute for Chemical Physics of Solids, Nöthnitzer Strasse 40, 01187 Dresden, Germany*
[7]*Department of Quantum Matter Physics, University of Geneva, 24 Quai Ernest-Ansermet, CH-1211 Geneva, Switzerland*

(Received 12 July 2024; accepted 4 October 2024; published 12 November 2024)

Competing interactions in low-dimensional materials can produce nearly degenerate electronic and structural phases. We investigate structural phase transitions in layered $IrTe_2$ for which a number of potential transition mechanisms have been postulated. The spatial coexistence of multiple phases on the micron scale has prevented a detailed analysis of the electronic structure. By exploiting micro-angle-resolved photoemission spectroscopy obtained with synchrotron radiation we extract the electronic structure of the multiple structural phases in $IrTe_2$ in order to address the mechanism underlying the phase transitions. We find direct evidence of lowered energy states that appear in the low-temperature phases, states previously predicted by *ab initio* calculations and extended here. Our results validate a proposed scenario of bonding and antibonding states as the driver of the phase transitions.

DOI: 10.1103/PhysRevB.110.205123

The diversity of electronic and magnetic phenomena occurring in quasi-two-dimensional (2D) transition metal dichalcogenides (TMDs) can largely be traced back to the presence of a partially filled d valence band [1]. The relatively narrow d bands, with widths on the same order as the Coulomb interaction, produce ideal conditions for correlated phenomena such as superconductivity [2–4], metal-insulator transitions [5], and charge density waves (CDWs) beyond the Peierls paradigm [6–8].

Here we focus on the unusual structural transitions in the well-known TMD $IrTe_2$ involving Ir atoms formally in a $5d^6$ electronic configuration. Already at 280 K the crystal structure of $IrTe_2$ transitions from a trigonal $1T$ phase (P-$3m1$) to a monoclinic (P-1) $5\times1\times5$ superstructure in a first-order fashion [9]. In the bulk this is followed by a second transition at 180 K into an $8\times1\times8$ phase [10]. Low-temperature (LT) measurements have revealed a $6\times1\times6$ ground state [11,12], which can also be stabilized in Se doped [13] and uniaxially strained crystals [14]. Although the resistivity is reduced in the LT phases, $IrTe_2$ remains metallic at all temperatures. Each of the phases below 280 K exhibits a shortening of some of the Ir-Ir distances within the unit cell into effective dimers [15]. The number of these Ir dimers within a unit cell is characteristic to each of the LT phases [10,16] [see Figs. 1(a) and 1(b)]. Furthermore, in monolayer samples a novel insulating 2×1 behavior has been observed [17]. Determining the mechanism of the structural transitions is therefore an important task.

Initially proposed weak-coupling scenarios based on Fermi nesting [9] appear to be incompatible with the dramatic 20% reduction in Ir bond lengths later observed in the LT phases [15]. Alternative scenarios include a $J_{\text{eff}} = 1/2$ spin-orbit Mott state [10], similar to that observed in Sr_2IrO_4 [18], proposed to arise due to a possible Ir $5d^5$ (Ir^{4+}) configuration in the LT phases. A number of works have put forward ideas based on a molecular-type picture involving either depolymerisation between the layers [13] or an effective Ir dimerization that produces bonding and antibonding $5d$ states [15,19] [see Fig. 1(c)] as part of a more complex multicenter bond [20]. Further support for this scenario was obtained by recent high-pressure diffraction measurements, where an observed modification of the Ir-Te angle provides conditions compatible with a ring-shaped bond across multiple sites [21]. In both the LT and high-pressure calculations, the predicted bonding states appear distinctly split off to higher binding energies from the density of states (DOS) of the remaining undimerized Ir atoms. Direct experimental confirmation of such states has not been obtained.

Validation or falsification of this scenario therefore requires clear electronic structure data, e.g., from angle-resolved photoemission spectroscopy (ARPES). Numerous studies have provided insights into the electronic structure of $IrTe_2$

*Contact author: cw_nicholson@protonmail.com
†Contact author: claude.monney@unifr.ch

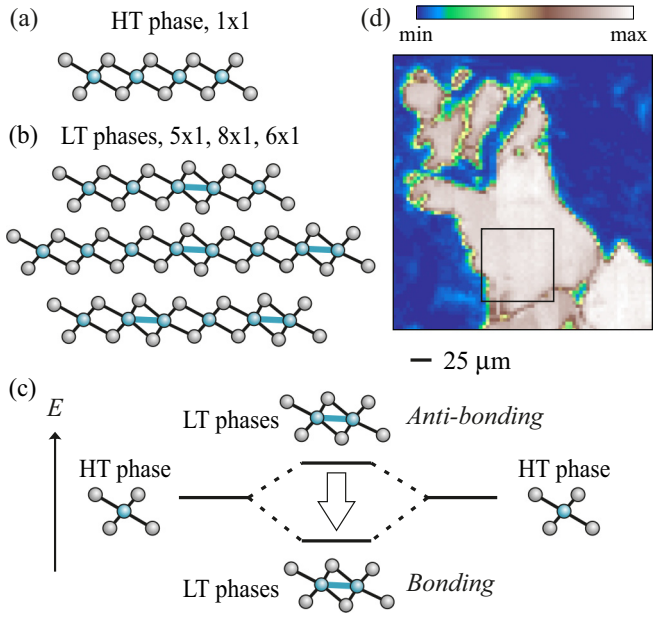

FIG. 1. (a) Side view of the crystal structure of $1T$-$IrTe_2$ in the high-temperature (HT) 1×1 phase and (b) in the various LT phases (top row 5×1, middle row 8×1, bottom row 6×1). (c) Schematic bonding energy level diagram in the HT and LT phases, highlighting the formation of bonding states due to the dimer bonds. (d) Overview image of the sample obtained with micro-ARPES with a pixel size of 5 µm. Blue color corresponds to the background signal from the epoxy used to glue the sample.

[10,14,16,22–29]. However, extraction of the intrinsic electronic structure is complicated by the spatial coexistence of a ladder of nearly degenerate phases with periodicity $3n+2$ ($n=1,2,3,\ldots$) at the surface with 5×1, 8×1, and 6×1 the dominant phases in observations [11]. Typical domain sizes ($\approx$10 µm [27]) are beyond the reach of most ARPES setups, with the result that only the 6×1 phase has been unambiguously isolated with strain ARPES [14]. An outstanding issue is therefore to address the electronic structure in the intrinsic LT structures without extraneous influence.

We overcome this challenge by applying micro-ARPES and micro-XPS (x-ray photoemission spectroscopy) with synchrotron radiation to $IrTe_2$ in order to isolate the electronic structure of the surface 5×1, 8×1, and 6×1 phases. Individual phases are identified by their characteristic Ir $4f$ core level spectra, allowing us to determine the spatial extent of domains on the micrometer scale, and to extract the intrinsic band structure of individual phases with ARPES. We observe split-off states in the DOS of the LT phases, clearly supporting a bonding mechanism for the phase transition.

Single crystals of $IrTe_2$ were grown using the self-flux method [30,31] and were characterized by magnetic susceptibility and resistivity measurements [16]. Micro-ARPES and micro-XPS measurements were carried out on the nanobranch of the I05 beamline at Diamond Light Source with a hemispherical analyzer in a base pressure of low 10^{-10} mbar. For these measurements we selected beam sizes produced by a microfocusing capillary in order to achieve a spot size of around 6 µm (full width at half maximum) with high photon flux on the sample. This configuration was chosen to allow efficient probing of the typical domain sizes [27]. All data were obtained with p-polarized light. The ARPES measurements shown here were carried out between 70 and 90 eV, while XPS was obtained at a photon energy of 130 eV due to the increased Ir $4f$ cross section. All crystals were cleaved in vacuum using a ceramic top post.

The density functional theory DOS calculations were performed using the Vienna *Ab Initio* Simulation Package (VASP) [32–35] within the projector augmented wave method [36] and the generalized gradient approximation using the Perdew-Burke-Ernzerhof functional [37]. The kinetic energy cutoff was set to 400 eV and the Brillouin zone was sampled with the tetrahedron method [38] and a Γ-centered k-point grid with spacing 0.08 $Å^{-1}$. Spin-orbit interaction was included in all calculations.

A large scale micro-ARPES map of an $IrTe_2$ sample obtained at 50 K with 5-µm step size is shown in Fig. 1(d). The image is produced by integrating the ARPES intensity over the full detector, and represented according to the color scale shown. We focus on the area highlighted by the black rectangle in order to perform more detailed mapping, as multiple phases are found within the scan area. We initially carried out an XPS map in order to determine the distribution of phases at a sample temperature of 160 K, i.e., below the nominal 5×1–8×1 transition. Since the ratio of dimer (Ir_d) to monomer (Ir_m) iridium atoms is different in each LT phase, each phase has a characteristic ratio $R = Ir_d/(Ir_m+Ir_d)$ of the integrated intensity under the XPS peak corresponding to those two separate Ir environments [16], e.g., in the different Ir $4f_{7/2}$ peaks. Thus the ratio is 2/5 (0.4) for the 5×1 phase, 4/8 (0.5) for the 8×1 phase, and 4/6 (0.67) in the 6×1 phase [see Fig. 1(c)]. Exemplary individual XPS spectra of the $4f_{7/2}$ core level for each LT phases are presented in Fig. 2(a), revealing the strong increase of the dimer signal at 61.5 eV in the 8×1 and 6×1 phases, in comparison to the 5×1 phase. The unusual linear background is due to the particular response of the analyzer detector in fixed mode (used for XPS only). The ratio is obtained from the XPS data by fitting with a two-peak Voigt function on a linear background and a constant offset [see Fig. 2(b)]. The resulting spatial ratio plot of R is shown in Fig. 2(c). From the color scale it is evident that all three phases coexist at this temperature, which is somewhat surprising given that in the bulk the 5×1 and 8×1 phases do not coexist [10]. Nevertheless, this is in good agreement with our previous photoemission study indicating coexistence of different phases at low temperature at the surface [16]. The XPS spatial map is dominated by regions with R values near 0.4 and 0.5, indicating dominantly 5×1 and 8×1 phases. The gradual variation in the color scale near domain boundaries suggests a partial mixing of phases within the selected spatial resolution.

The spatial distribution of phases obtained from the XPS data also allows us to probe the individual LT phases with ARPES; the results obtained at 160 K along the H-A-H direction and the K-Γ-K direction of the bulk Brillouin zone of the high-temperature (HT) phase are shown in Fig. 3. A global similarity can be observed between all phases, including the 1×1 phase obtained at room temperature [Fig. 3(a)]. Notable features in the 1×1 phase that are carried over to the LT phase include the intense band dispersing from -2 eV at the zone

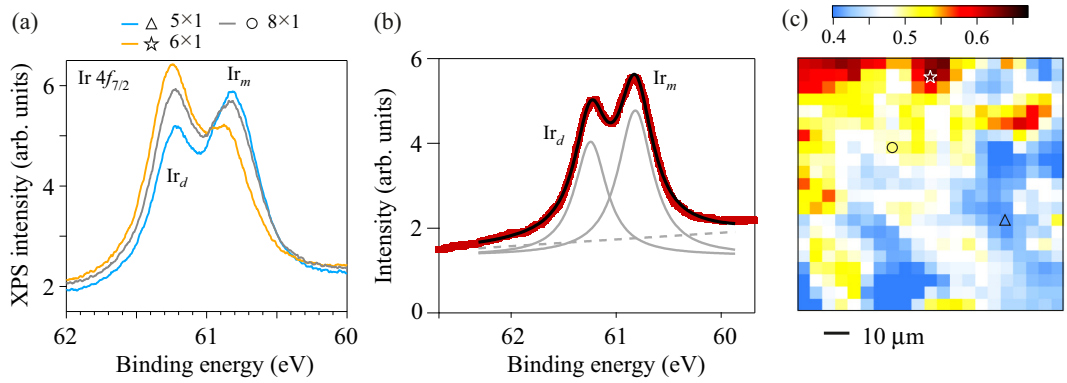

FIG. 2. (a) XPS spectra of the 4$f_{7/2}$ core level obtained from specific domains with a single phase [the individual positions are indicated by markers in (c)]. (b) Exemplary fit of the Ir 4$f_{7/2}$ core level in the 5×1 phase. The fit function is composed of the sum of two Voigt peaks on top of a linear background and a constant offset. Individual component curves and the background are shown. The spectral weight under each peak is extracted and used to plot the ratio of peaks in (c). (c) XPS map of the region highlighted (black rectangle) in Fig. 1(d) obtained at 160 K and 130-eV photon energy. The color scale encodes the proportion (R) of Ir$_d$ relative to the total population of Ir atoms, $R = \mathrm{Ir}_d/(\mathrm{Ir}_m+\mathrm{Ir}_d)$. The observed R values for the three spectra shown in (a) are 0.64 (star), 0.50 (circle), and 0.41 (triangle).

boundary to the Fermi level, and the topological surface state [39] with an energy of −1 eV at the zone center, which is shifted to higher binding energies in the LT phases [16].

However, distinct differences are observed across the energy window in the LT phases, particularly in the region close to the Fermi level. In the 5×1 phase [Fig. 3(b)] mirror symmetry is broken (the corresponding low-symmetry space group is P-1), as seen from the states off center around −0.3 eV at $k_{\mathrm{HAH}} = \pm 0.6$ Å^{-1} (see arrows). In addition, in each of the LT phases, the bottoms of the bulk Dirac states, unoccupied in the 1×1 phase, are now shifted into the occupied states at the zone center [see the horizontal arrows in

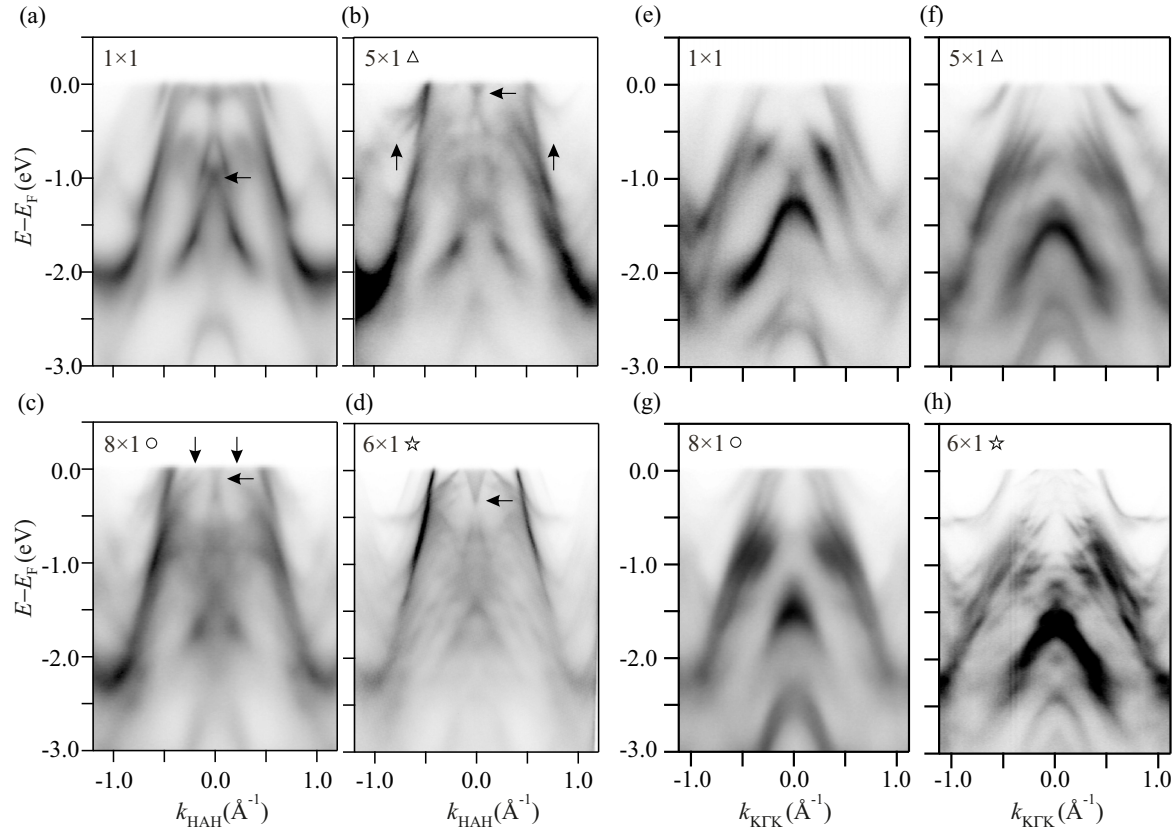

FIG. 3. Experimental band structure at the bulk A point (90-eV photon energy) along the high-symmetry direction HAH of the HT Brillouin zone in the (a) 1×1, (b) 5×1, (c) 8×1, and (d) 6×1 phase. Arrows mark the key features described in the text. Experimental band structure at the bulk Γ point (70-eV photon energy) along the high-symmetry direction $K\Gamma K$ of the HT Brillouin zone in the (e) 1×1, (f) 5×1, (g) 8×1, and (h) 6×1 phase. All spectra, except for those of graphs (a) and (e) (which are taken at RT) are obtained at the points marked in Fig. 2, and at a temperature of 160 K.

Figs. 3(b)–3(d)]. This feature is similar in the 5×1 and 8×1 [Figs. 3(b) and 3(c)] phases, but the hyperbolic dispersion only becomes evident in the 6×1 phase [Fig. 3(d)] as previously observed [14]. A clear difference between the 5×1 and 8×1 phases is observed close to the zone center. Between the Dirac states and the intense band dispersing to −2 eV, only a single band is observed dispersing to the Fermi level in the 5×1 phase. In contrast the 8×1 phase shows two states dispersing to the Fermi level, which may be a result of the broken inversion symmetry of this phase that is expected to lift the spin degeneracy [15]. For completeness, the 6×1 phase appears identical to that obtained in strained samples [14]. We also observe that globally the band structure of the 6×1 phase is much sharper than that of the other phases. As a possible explanation, we notice that scanning tunneling microscopy images of these different phases exhibit substantially less disorder in the dimer periodicity of the 6×1 phase compared to the other phases [40,41]. In contrast to a previous study [10] we do not find evidence for the appearance of a flat band at Γ below 280 K and instead find a dispersing band in the expected region along the high symmetry direction $K\Gamma K$ [Figs. 3(f)–3(h)]. The corresponding ARPES data for the 1×1 phase is shown in Fig. 3(e). Since a nondispersing state is expected for the spin-orbit Mott state, we therefore conclude that a Mott phase in $IrTe_2$ is unlikely. This difference compared to the previous work may be due to the specially chosen spatial resolution used in the current paper, removing any influence from a mixture of domains with different orientations or from other phases.

As mentioned above, the energy of the topological surface state is shifted to higher binding energies compared with the 1×1 phase. The value of the shift is −0.37 eV (5×1), −0.34 eV (8×1), and −0.46 eV (6×1) for the three LT phases. These values are slightly larger, but with the same trend, as previously determined values employing larger beam sizes in ARPES measurements [16]. This shift of the surface state implies a lowered energy configuration in the LT states, which foreshadows the observation of bulk bonding states discussed in more detail below.

Given the suggestive behavior of the surface states, we investigated the split-off bonding DOS predicted by bulk DFT calculations in the region of −3-eV binding energy [15]. In order to better compare the momentum-resolved experimental data with the predicted DOS, we have calculated the orbital-resolved DOS within a small momentum range close to the zone center (Γ point) to avoid including the highly dispersive states at higher momenta present at all temperatures. We use a pseudocubic axis system with the x and y axes pointing approximately along the Ir-Te bond directions, such that the Ir d_{xy} orbitals are directed along the dimer bonds. The 1×1 phase is dominated by the Ir d orbitals as can be seen in Fig. 4(a). In the following, we focus on the d_{xy} orbital in the 5×1 phase, since the d_{xy} orbitals overlap directly in the formation of the Ir dimers, resulting in large binding energy shifts, as previously addressed by Pascut *et al.* [15]. The 5×1 phase is chosen due its smaller unit cell compared with the 8×1, and the fact that structural data for the intrinsic 6×1 phase are not available [13,15,21]. The three curves in Fig. 4(b) reflect the three inequivalent Ir sites in the 5×1 phase: dimerized atoms and two species of monomers depending on their proximity to

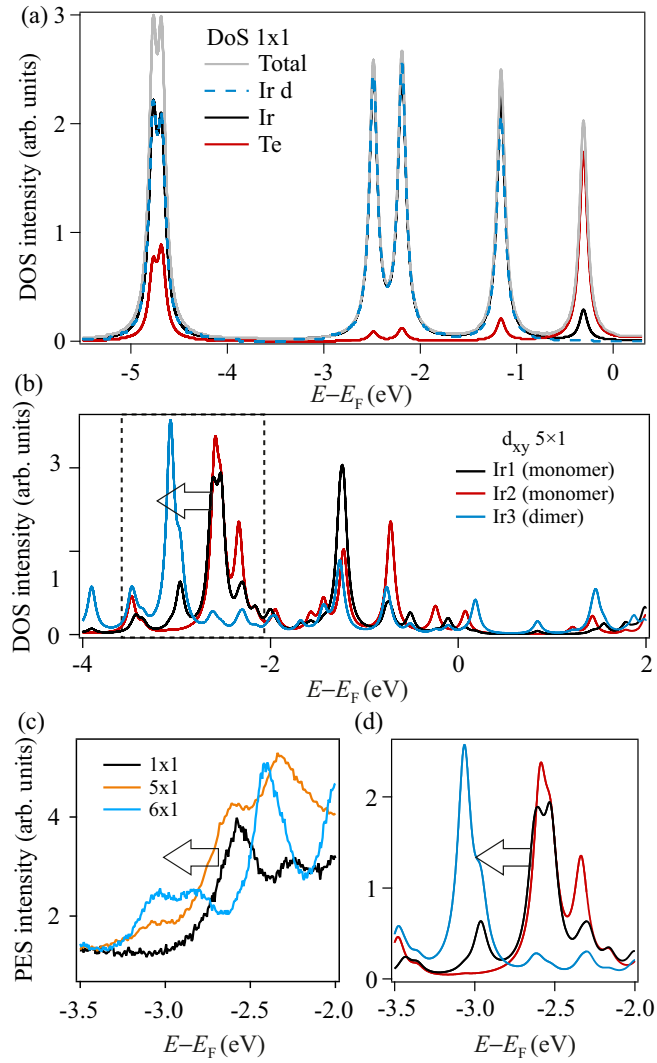

FIG. 4. (a) Calculated partial DOS in the 1×1 phase for all atoms, for Te atoms only, for Ir atoms only, and for the d orbitals of the Ir atoms only. A pseudocubic axis system was used with the x and y axes pointing approximately along the Ir-Te bond directions, such that the Ir d_{xy} orbitals are directed along the dimer bonds. (b) Calculated partial DOS in the 5×1 phase for the d_{xy} orbital for the different Ir environments. (c) Experimental spectra extracted at $k_{K\Gamma K} = 0$ and normalized to the intensity at −3.5 eV in the 1×1, 5×1, and 6×1 phases. Data are obtained at 70 eV, corresponding to the bulk Γ point. (d) Magnification of the region shown in (c) for the calculated partial DOS.

the dimers. A distinct shift of the dimer DOS to 0.5-eV lower binding energy compared with the monomers is observed. We note here that a similar behavior is observed in the d_{yz} and d_{xz} orbitals. These split-off states are the fingerprints of bonding state formation as proposed by previous works [15,20]. Corresponding antibonding states are predicted above the Fermi level at around 1.5 eV [see Ref. [20] and Fig. 4(b)]. Our result is similar to the previous calculations, although it displays a clearer effect due to the selective momentum range applied. We note that similar split-off states are expected also at other binding energies below the range currently under investigation [20].

To compare directly with the calculated DOS, we extract an energy slice at the zone center (Γ point) from ARPES measurements, presented in Fig. 4(c). The energy range is chosen to encompass the DOS states highlighted in Fig. 4(b) which have already been shown to be of most relevance. In the 1×1 data (black curve) the tail of the DOS extends to −3 eV, but no peaks are observed in this region. In contrast, in the 5×1 phase a clear peak is evident at −3.05 eV, with a difference in energy of −0.46 eV compared with the lowest energy peak in the 1×1 phase. This peak becomes even more pronounced in the 6×1 phase, with a double peak structure forming that mirrors that of the DOS calculation. The ARPES data therefore provide direct evidence for states split off from the 1×1 DOS associated with the LT phases.

The observation of split-off states in the LT phases, at energies well separated from the 1×1 DOS, is in excellent agreement with the prediction from our momentum-selective calculations, and fully compatible with the previous momentum-integrated calculations. The close correspondence of experiment and theory therefore provides direct evidence for bonding state formation tied to the structural transition, validating a scenario of strongly bonded atoms as the driver of the structural phase transition [15,20]. Indeed, such a scenario provides a natural alternative to the formation of an electronic gap, which is not observed in $IrTe_2$ and where a metallic, albeit reduced, DOS at the Fermi level is always observed in the LT phases. The large energetic shifts of 0.5 eV in $IrTe_2$ are comparable to but larger than the typical electronic energy gains in quasi-2D CDW materials [8].

The observed split-off states are clearly associated with bulk Ir 5*d* states, and are far removed from the surface states in energy. This confirms that the electronic structure differences observed here with ARPES are representative of the bulk transition. We note that this situation may not hold in very thin samples, where a number of additional phenomena are observed, including an enhanced transition temperature for the 5×1 phase [42] and a coexistence of structural 5×1 order and superconductivity [43]. These observations further imply that the out-of-plane bonding is involved in the phase transition. Indeed, the role of the Te-Te bond was already discussed in early works to explain the anomalously small c/a ratio [30,44], and the results of Se doping [13]. In fact, a reduction of interlayer bond strength is an additional consequence of the multicenter bond formed in the LT phases [20], and is supported by the reduced interlayer coupling observed in ARPES of the 6×1 phase [14]. This highlights that the picture of the dimer motif forming bonding states provides a coherent description of the observed data for the structural transitions in $IrTe_2$.

In summary, we used synchrotron micro-ARPES to separate the intrinsic electronic structure of the micro-scale LT phases in $IrTe_2$. The rich structures unveiled display mirror symmetry breaking in the 5×1 phase, and possible features of inversion symmetry breaking in the 8×1 phase. The structure of the 6×1 phase appears to be equivalent to that stabilized under uniaxial strain. Disentangling the various phases allowed us to resolve split-off bonding states that appear in the LT phases at around −3-eV binding energy, as previously predicted based on structural models. Our DOS calculations confirm the appearance of these states in terms of d_{xy}, d_{yz}, d_{xz}, and $d_{x^2-y^2}$ orbitals. Our results provide experimental evidence for a mechanism based on short dimer bonds as the energetic driver of the structural transitions in layered $IrTe_2$.

This project was supported by Swiss National Science Foundation Grant No. P00P2_170597. This work was supported by the project Quantum materials for applications in sustainable technologies (QM4ST), funded as Project No. CZ.02.01.01/00/22_008/0004572 by Programme Johannes Amos Comenius, call Excellent Research. We thank Diamond Light Source for access to beamline I05 under Proposal No. SI25906.

[1] J. A. Wilson and A. D. Yoffe, The transition metal dichalcogenides discussion and interpretation of the observed optical, electrical and structural properties, Adv. Phys. **18**, 193 (1969).

[2] E. Revolinsky, E. P. Lautenschlager, and C. H. Armitage, Layer structure superconductor, Solid State Commun. **1**, 59 (1963).

[3] E. Morosan, H. W. Zandbergen, B. S. Dennis, J. W. G. Bos, Y. Onose, T. Klimczuk, A. P. Ramirez, N. P. Ong, and R. J. Cava, Superconductivity in Cu_xTiSe_2, Nat. Phys. **2**, 544 (2006).

[4] B. Sipos, A. F. Kusmartseva, A. Akrap, H. Berger, L. Forró, and E. Tutis, From Mott state to superconductivity in 1T-TaS_2, Nat. Mater. **7**, 960 (2008).

[5] P. Fazekas and E. Tosatti, Electrical, structural and magnetic properties of pure and doped 1T-TaS_2, Philos. Mag. B **39**, 229 (1979).

[6] J. A. Wilson, Bands, bonds, and charge-density waves in the $NbSe_3$ family of compounds, Phys. Rev. B **19**, 6456 (1979).

[7] H. Cercellier *et al.*, Evidence for an excitonic insulator phase in 1T-$TiSe_2$, Phys. Rev. Lett. **99**, 146403 (2007).

[8] K. Rossnagel, On the origin of charge-density waves in select layered transition-metal dichalcogenides, J. Phys.: Condens. Matter **23**, 213001 (2011).

[9] J. J. Yang, Y. J. Choi, Y. S. Oh, A. Hogan, Y. Horibe, K. Kim, B. I. Min, and S. W. Cheong, Charge-orbital density wave and superconductivity in the strong spin-orbit coupled $IrTe_2$:Pd, Phys. Rev. Lett. **108**, 116402 (2012).

[10] K. T. Ko, H. H. Lee, D. H. Kim, J. J. Yang, S. W. Cheong, M. J. Eom, J. S. Kim, R. Gammag, K. S. Kim, H. S. Kim, T. H. Kim, H. W. Yeom, T. Y. Koo, H. D. Kim, and J. H. Park, Charge-ordering cascade with spin-orbit Mott dimer states in metallic iridium ditelluride, Nat. Commun. **6**, 7342 (2015).

[11] P.-J. Hsu, T. Mauerer, M. Vogt, J. J. Yang, Y. S. Oh, S.-W. Cheong, M. Bode, and W. Wu, Hysteretic melting transition of a soliton lattice in a commensurate charge modulation, Phys. Rev. Lett. **111**, 266401 (2013).

[12] K. Takubo, K. Yamamoto, Y. Hirata, H. Wadati, T. Mizokawa, R. Sutarto, F. He, K. Ishii, Y. Yamasaki, H. Nakao, Y. Murakami, G. Matsuo, H. Ishii, M. Kobayashi, K. Kudo, and M. Nohara, Commensurate versus incommensurate charge ordering near the superconducting dome in $Ir_{1-x}Pt_xTe_2$ revealed by resonant x-ray scattering, Phys. Rev. B **97**, 205142 (2018).

[13] Y. S. Oh, J. J. Yang, Y. Horibe, and S. W. Cheong, Anionic depolymerization transition in $IrTe_2$, Phys. Rev. Lett. **110**, 127209 (2013).

[14] C. W. Nicholson, M. Rumo, A. Pulkkinen, G. Kremer, B. Salzmann, M.-l. Mottas, B. Hildebrand, T. Jaouen, T. K. Kim, S. Mukherjee, K. Ma, M. Muntwiler, F. O. V. Rohr, C. Cacho, and C. Monney, Uniaxial strain-induced phase transition in the 2D topological semimetal $IrTe_2$, Commun. Mater. **2**, 25 (2021).

[15] G. L. Pascut, K. Haule, M. J. Gutmann, S. A. Barnett, A. Bombardi, S. Artyukhin, T. Birol, D. Vanderbilt, J. J. Yang, S. W. Cheong, and V. Kiryukhin, Dimerization-induced cross-layer quasi-two-dimensionality in metallic $IrTe_2$, Phys. Rev. Lett. **112**, 086402 (2014).

[16] M. Rumo *et al.*, Examining the surface phase diagram of $IrTe_2$ with photoemission, Phys. Rev. B **101**, 235120 (2020).

[17] J. Hwang, K. Kim, C. Zhang, T. Zhu, C. Herbig, S. Kim, B. Kim, Y. Zhong, M. Salah, M. M. El-Desoky, C. Hwang, Z. X. Shen, M. F. Crommie, and S. K. Mo, Large-gap insulating dimer ground state in monolayer $IrTe_2$, Nat. Commun. **13**, 906 (2022).

[18] B. J. Kim, H. Jin, S. J. Moon, J. Y. Kim, B. G. Park, C. S. Leem, J. Yu, T. W. Noh, C. Kim, S. J. Oh, J. H. Park, V. Durairaj, G. Cao, and E. Rotenberg, Novel $J_{\text{eff}} = 1/2$ Mott state induced by relativistic spin-orbit coupling in Sr_2IrO_4, Phys. Rev. Lett. **101**, 076402 (2008).

[19] G. L. Pascut, T. Birol, M. J. Gutmann, J. J. Yang, S. W. Cheong, K. Haule, and V. Kiryukhin, Series of alternating states with unpolarized and spin-polarized bands in dimerized $IrTe_2$, Phys. Rev. B **90**, 195122 (2014).

[20] G. Saleh and S. Artyukhin, First-principles theory of phase transitions in $IrTe_2$, J. Phys. Chem. Lett. **11**, 2127 (2020).

[21] T. Ritschel, Q. Stahl, M. Kusch, J. Trinckauf, G. Garbarino, V. Svitlyk, M. Mezouar, J. Yang, S. W. Cheong, and J. Geck, Local mechanism of valence bond formation in $IrTe_2$, arXiv:2112.04584.

[22] D. Ootsuki, S. Pyon, K. Kudo, M. Nohara, M. Horio, T. Yoshida, T. Oshida, A. Fujimori, M. Arita, H. Anzai, H. Namatame, M. Taniguchi, N. L. Saini, and T. Mizokawa, Electronic structure reconstruction by orbital symmetry breaking in $IrTe_2$, J. Phys. Soc. Jpn. **82**, 093704 (2013).

[23] D. Ootsuki, H. Ishii, K. Kudo, M. Nohara, M. Takahashi, M. Horio, A. Fujimori, T. Yoshida, M. Arita, H. Anzai, H. Namatame, M. Taniguchi, N. L. Saini, and T. Mizokawa, A novel one-dimensional electronic state at $IrTe_2$ surface, J. Phys. Soc. Jpn. **86**, 123704 (2017).

[24] T. Qian, H. Miao, Z. J. Wang, X. Shi, Y. B. Huang, P. Zhang, N. Xu, L. K. Zeng, J. Z. Ma, P. Richard, M. Shi, G. Xu, X. Dai, Z. Fang, A. F. Fang, N. L. Wang, and H. Ding, Structural phase transition associated with van Hove singularity in 5*d* transition metal compound $IrTe_2$, New J. Phys. **16**, 123038 (2014).

[25] S. F. Blake, M. D. Watson, A. McCollam, S. Kasahara, R. D. Johnson, A. Narayanan, G. L. Pascut, K. Haule, V. Kiryukhin, T. Yamashita, D. Watanabe, T. Shibauchi, Y. Matsuda, and A. I. Coldea, Fermi surface of $IrTe_2$ in the valence-bond state as determined by quantum oscillations, Phys. Rev. B **91**, 121105(R) (2015).

[26] H. Lee, K. T. Ko, K. Kim, B. G. Park, J. Yang, S. W. Cheong, and J. H. Park, Electronic reconstruction on dimerized $IrTe_2$, Europhys. Lett. **120**, 47003 (2017).

[27] C. Bao, H. Zhang, Q. Li, S. Zhou, H. Zhang, K. Deng, K. Zhang, L. Luo, W. Yao, C. Chen, J. Avila, M. C. Asensio, Y. Wu, and S. Zhou, Spatially-resolved electronic structure of stripe domains in $IrTe_2$ through electronic structure microscopy, Commun. Phys. **4**, 229 (2021).

[28] M. Rumo, A. Pulkkinen, B. Salzmann, G. Kremer, B. Hildebrand, K. Y. Ma, F. O. Von Rohr, C. W. Nicholson, T. Jaouen, and C. Monney, Insensitivity of the striped charge orders in $IrTe_2$ to alkali surface doping implies their structural origin, Phys. Rev. Mater. **5**, 074002 (2021).

[29] T. Mizokawa, A. Barinov, V. Kandyba, A. Giampietri, R. Matsumoto, Y. Okamoto, K. Takubo, K. Miyamoto, T. Okuda, S. Pyon, H. Ishii, K. Kudo, M. Nohara, and N. L. Saini, Domain dependent Fermi arcs observed in a striped phase dichalcogenide, Adv. Quantum Technol. **5**, 2200029 (2022).

[30] S. Jobic, P. Deniard, R. Brec, and J. Rouxel, Crystal and electronic band structure of $IrTe_2$: Evidence of anionic bonds in a CdI_2-like arrangement, Z. Anorg. Allg. Chem. **598**, 199 (1991).

[31] A. F. Fang, G. Xu, T. Dong, P. Zheng, and N. L. Wang, Structural phase transition in $IrTe_2$: A combined study of optical spectroscopy and band structure calculations, Sci. Rep. **3**, 1153 (2013).

[32] G. Kresse and J. Hafner, *Ab initio* molecular dynamics for liquid metals, Phys. Rev. B **47**, 558 (1993).

[33] G. Kresse and J. Hafner, *Ab initio* molecular-dynamics simulation of the liquid-metalamorphous-semiconductor transition in germanium, Phys. Rev. B **49**, 14251 (1994).

[34] G. Kresse and J. Furthmüller, Efficiency of *ab-initio* total energy calculations for metals and semiconductors using a plane-wave basis set, Comput. Mater. Sci. **6**, 15 (1996).

[35] G. Kresse and J. Furthmüller, Efficient iterative schemes for *ab initio* total-energy calculations using a plane-wave basis set, Phys. Rev. B **54**, 11169 (1996).

[36] G. Kresse and D. Joubert, From ultrasoft pseudopotentials to the projector augmented-wave method, Phys. Rev. B **59**, 1758 (1999).

[37] J. P. Perdew, K. Burke, and M. Ernzerhof, Generalized gradient approximation made simple, Phys. Rev. Lett. **77**, 3865 (1996).

[38] P. E. Blöchl, Projector augmented-wave method, Phys. Rev. B **50**, 17953 (1994).

[39] M. S. Bahramy *et al.*, Ubiquitous formation of bulk Dirac cones and topological surface states from a single orbital manifold in transition-metal dichalcogenides, Nat. Mater. **17**, 21 (2018).

[40] J. Dai, K. Haule, J. J. Yang, Y. S. Oh, S. W. Cheong, and W. Wu, Hierarchical stripe phases in $IrTe_2$ driven by competition between Ir dimerization and Te bonding, Phys. Rev. B **90**, 235121 (2014).

[41] C. Chen, J. Kim, Y. Yang, G. Cao, R. Jin, and E. W. Plummer, Surface phases of the transition-metal dichalcogenide $IrTe_2$, Phys. Rev. B **95**, 094118 (2017).

[42] Y. Song, F. Meng, T. Ying, J. Deng, J. Wang, X. Han, Q. Zhang, Y. Huang, J. G. Guo, and X. Chen, Spatially separated superconductivity and enhanced charge-density-wave ordering in an $IrTe_2$ nanoflake, J. Phys. Chem. Lett. **12**, 12180 (2021).

[43] S. Park, S. Y. Kim, H. K. Kim, M. J. Kim, T. Kim, H. Kim, G. S. Choi, C. J. Won, S. Kim, K. Kim, E. F. Talantsev, K. Watanabe, T. Taniguchi, S. W. Cheong, B. J. Kim, H. W. Yeom, J. Kim, T. H. Kim, and J. S. Kim, Superconductivity emerging from a stripe charge order in $IrTe_2$ nanoflakes, Nat. Commun. **12**, 3157 (2021).

[44] S. Jobic, R. Brec, and J. Rouxel, Anionic polymeric bonds in transition metal ditellurides, J. Solid State Chem. **96**, 169 (1992).